Progress In Electromagnetics Research M, Vol. 48, 45–54, 2016

Near-Ground Transient Field of a High-Altitude Electromagnetic Pulse (HEMP) Considering Nonlinear Air Conductivity and Ground Reflection

Hong-Cheng Wei and Jean-Fu Kiang

Abstract—Transient field of a high-altitude electromagnetic pulse (HEMP) induced near ground is simulated, of which the ground reflection can not be neglected. The Jefimenko's equation is applied to compute the incident electric field near the ground, attributed to both the primary and the secondary currents in the source region. The field-dependent air conductivity in the source region is obtained by solving three nonlinear governing equations iteratively, and the reflected field is computed in the frequency domain.

1. INTRODUCTION

The γ rays generated by a high-altitude nuclear explosion strike air molecules in the upper atmosphere, producing Compton electrons which move almost in parallel to the γ rays and constitute a primary current [1, 2]. The Compton electrons also ionize air molecules, creating secondary electrons which in turns modify the effective conductivity of the atmosphere [2, 3]. The electromagnetic field radiated by the primary current, under the influence of the air conductivity, is conventionally called a high-altitude electromagnetic pulse (HEMP).

The Lienard-Wiechert potentials were used to compute HEMPs radiated by the primary current [4], where only the synchrotron radiation was considered, while the radiation attributed to frictional losses (Bremsstrahlung radiation) was neglected. In [5], HEMP was computed by using the Jefimenko's equation as well as the CHAP's code [3]. The characteristics of electric fields attributed to primary and secondary currents were also discussed. In [6], the electric field of early-time HEMP was simulated with different heights of burst (HOBs), explosive yields and observation locations.

The effective conductivity in the source region is nonlinearly related to the in situ electric field, which can significantly affect the accuracy of simulated HEMP waveform near ground. In this work, we propose an iterative method to compute both the electric field and the air conductivity distributions in the source region. The incident electric field near ground is then computed by applying the Jefimenko's equation to both the primary and the secondary currents.

When the near-ground transient field in the first millisecond is concerned, reflected field components are mingled with the incident field components radiated from the portion of source region away from the line-of-sight path. The electric field reflected by the ground is computed by transforming the incident field to the frequency domain and multiplying with the frequency-dependent reflection coefficient, then transforming back to the time domain.

This paper is organized as follows: The theory to compute the primary current is briefly reviewed in Section 2, the method of solving for the air conductivity and the secondary current is presented in Section 3, the method to compute the reflected field is presented in Section 4, and simulation results are discussed in Section 5. Finally, some conclusions are drawn in Section 6.

Received 19 February 2016, Accepted 16 April 2016, Scheduled 26 April 2016

* Corresponding author: Jean-Fu Kiang (jfkiang@ntu.edu.tw).

The authors are with the Department of Electrical Engineering and the Graduate Institute of Communication Engineering, National Taiwan University, Taipei 106, Taiwan, R.O.C.

2. COMPUTATION OF PRIMARY CURRENT

Figure 1 shows the coordinate systems used to compute the electric field distribution of an HEMP. The burst point, which is at a height of h above the ground, is chosen as the origin O' of the (x', y', z') coordinates, with the z' axis aligned with the local geomagnetic field. The (x, y, z) coordinates are defined to have the origin O lying directly below O', with the x and y axes pointing in the local east and north directions, respectively. A gamma ray propagates from O', over a distance r', to a point $\bar{r}_d$ in the source region. The source region is divided into small cubes labeled with indices $[m, n, \ell]$. The primary and secondary currents in a small cube centered at $\bar{r}_d$ will radiate electromagnetic wave, over a distance R, to an observation point $\bar{r}_s$ near the ground surface.

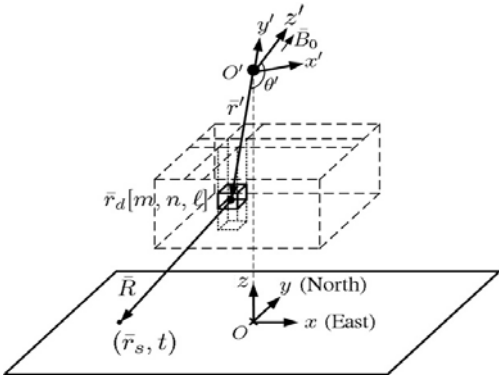

Figure 1. Coordinate systems for simulation of an HEMP.

The primary current density, under the influence of geomagnetic field, can be expressed as [2]

$$\begin{aligned}
J_{\mathrm{pri},r'}(\bar{r}', t') \simeq & -e\zeta v_0 g(\bar{r}') \int_0^{R_\gamma/v_0} d\tau'' \left(\cos^2\theta' + \sin^2\theta' \cos\omega_L\tau''\right) \\
& f\left(\tau' - (1-\beta\cos^2\theta)\tau'' + \beta\sin^2\theta \frac{\sin\omega_L\tau''}{\omega_L}\right) \\
J_{\mathrm{pri},\theta'}(\bar{r}', t') \simeq & -e\zeta v_0 g(\bar{r}') \int_0^{R_\gamma/v_0} d\tau'' \sin\theta'\cos\theta' \left(\cos\omega_L\tau'' - 1\right) \\
& f\left(\tau' - (1-\beta\cos^2\theta')\tau'' + \beta\sin^2\theta' \frac{\sin\omega_L\tau''}{\omega_L}\right) \\
J_{\mathrm{pri},\phi'}(\bar{r}', t') \simeq & -e\zeta v_0 g(\bar{r}') \int_0^{R_\gamma/v_0} d\tau'' \sin\theta' \sin\omega_L\tau'' \\
& f\left(\tau' - (1-\beta\cos^2\theta')\tau'' + \beta\sin^2\theta' \frac{\sin\omega_L\tau''}{\omega_L}\right)
\end{aligned} \tag{1}$$

where $e = 1.6 \times 10^{-19}$ coul is a natural unit of charge, $\zeta \simeq 1$; $v_0 = 0.95c\,\mathrm{m/s}$ is the velocity of primary electrons; c is the speed of light in free space; $\omega_L = eB_0/(\gamma_L m_e)$ is the cyclotron frequency; m_e is the electron mass; B_0 is the geomagnetic field; $\beta = v_0/c$ and $\gamma_L = 1/\sqrt{1-\beta^2}$; $t' = t - R/c$, $\tau' = t' - r'/c$ and $\tau'' = t' - t''$; t is the observation time at O, with the burst starting at $t = 0$. The electromagnetic wave observed at $(\bar{r}, t)$ is contributed by the currents at $(\bar{r}', t')$; t'' is the time when a γ ray strikes an air molecule to create a primary electron; $R_\gamma \simeq 3 \times 10^2 \rho_0/\rho\,(\mathrm{cm})$ is the mean distance a primary electron travels in the atmosphere before being absorbed by an ion; ρ and ρ_0 are the air densities at the height of interest and on the ground, respectively.

Figure 2 shows the typical waveform of a γ-ray burst, which is represented as [7]

$$f(t) = \frac{e^{-\alpha_1/t - \alpha_2 t} u(t)}{\displaystyle\int_0^\infty dt' e^{-\alpha_1/t' - \alpha_2 t'}}$$

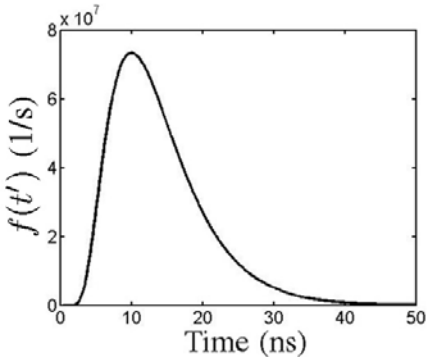

Figure 2. Typical waveform of a γ-ray burst [7].

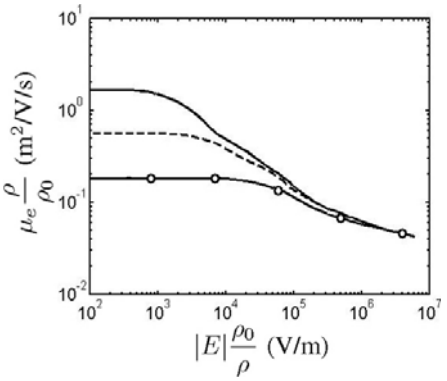

Figure 3. Electron mobility in air [8]; ——: $f_w = 0$, − − −: $f_w = 0.01$, − ∘ −: $f_w = 0.04$.

where $\alpha_1 = 2 \times 10^{-8}\,\mathrm{s}$ and $\alpha_2 = 2 \times 10^8\,\mathrm{s}^{-1}$ are empirical parameters. The $g(\bar{r}')$ function characterizes the generation of primary electrons, which is represented as [2, 7]

$$g(\bar{r}') = \frac{Y_\alpha}{E_{\mathrm{ray}}} \frac{\exp\left\{-\int_0^{\bar{r}'} dr/\ell_m\right\}}{4\pi r'^2 \ell_m}$$

where $\ell_m \simeq 3 \times 10^4 \rho_0/\rho\,(\mathrm{cm})$ is the mean free-path of primary electrons.

3. COMPUTATION OF AIR CONDUCTIVITY

The secondary current density takes the form of Ohm's law as [8]

$$\bar{J}_{\mathrm{sec}} = \sigma \bar{E} \tag{2}$$

where

$$\sigma(\bar{r}', t', |\bar{E}|) = e\mu_e(\bar{r}', |\bar{E}|) n_{\mathrm{sec}}(\bar{r}', t') \tag{3}$$

is the effective air conductivity [3], and μ_e is the electron mobility [8]. The number density of secondary electrons, under the influence of geomagnetic field, can be computed as [2, 6]

$$n_{\mathrm{sec}}(\bar{r}', t') \simeq -q\frac{v_0}{R_\alpha} g(\bar{r}') \int_{-\infty}^{\tau} e^{-k_1(\tau-\tau')} d\tau' \int_0^{R_\alpha/v_0} d\tau'' f\left(\tau' - (1-\beta\cos^2\theta)\tau'' + \beta\sin^2\theta \frac{\sin\omega_L\tau''}{\omega_L}\right) \tag{4}$$

where $k_1 = 10^8(\rho/\rho_0)^2\,\mathrm{s}^{-1}$ is the attachment rate of electrons to oxygen molecules [3]. Fig. 3 shows the electron mobility in the air, with the molecular fraction of water vapor being $f_w = 0, 0.01$ and 0.04, respectively [8].

The electric field in the source region satisfies the equation [2]

$$-\nabla'^2\bar{E} + \hat{r}'\frac{1}{c\epsilon_0}(\nabla'\cdot\bar{J}) + \frac{1}{\epsilon_0}\nabla'\rho_e + \frac{\partial}{\partial\tau'}\left[\frac{2}{cr'}\frac{\partial}{\partial r'}(r'\bar{E}) + \mu_0(\bar{J} - \hat{r}'J_{r'})\right] = 0 \tag{5}$$

where $\bar{J} = \bar{J}_{\mathrm{pri}} + \bar{J}_{\mathrm{sec}}$. Within the first 1 μs right after the burst ($\tau' \le 1\,\mu\mathrm{s}$), the spatial change rate of current is in general smaller than the temporal change rate [7], hence (5) can be approximated as

$$\frac{\partial}{\partial\tau'}\left[\frac{2}{cr'}\frac{\partial}{\partial r'}(r'\bar{E}) + \mu_0(\bar{J} - \hat{r}'J_{r'})\right] = 0 \tag{6}$$

Since μ_e is a function of the local electric field $\bar{E}$, (6) is a nonlinear equation of $\bar{E}$, and will be solved iteratively. First, we make an approximation that $\mu_e^{(0)} = 0.044\rho_0/\rho$, which is independent of $\bar{E}$.

The associated air conductivity becomes $\sigma^{(0)}(\bar{r}', t') = e\mu_e^{(0)}(\bar{r}')n_{\sec}(\bar{r}', t')$, which is also independent of the electric field. Then, the electric field is recomputed as

$$E_{r'}^{(1)}(\bar{r}', \tau') = -\frac{1}{\epsilon_0}\int_0^{\tau'} d\tau'' J_{\text{pri},r'}(\bar{r}', \tau'') \exp\left\{\frac{1}{\epsilon_0}\int_{\tau'}^{\tau''} d\tau''' \sigma^{(0)}(\bar{r}', \tau''')\right\} \tag{7}$$

$$E_{\alpha}^{(1)}(\bar{r}', \tau') = -\frac{c\mu_0}{2}\frac{1}{r'}\int_0^{r'} dr'' r'' J_{\text{pri},\alpha}(\bar{r}'', \tau') \exp\left\{-\frac{c\mu_0}{2}\int_{r''}^{r'} dr''' \sigma^{(0)}(\bar{r}''', \tau')\right\} \tag{8}$$

with $\alpha = \theta', \phi'$. The air conductivity is then updated as $\sigma^{(1)}(\bar{r}', t', |\bar{E}^{(1)}|) = e\mu_e^{(1)}(\bar{r}', |\bar{E}^{(1)}|)n_{\sec}(\bar{r}', t')$.

Alternatively, the electric field is iterated as

$$E_{r'}^{(n)}(\bar{r}', \tau') = -\frac{1}{\epsilon_0}\int_0^{\tau'} d\tau'' J_{\text{pri},r'}(\bar{r}', \tau'') \exp\left\{\frac{1}{\epsilon_0}\int_{\tau'}^{\tau''} d\tau''' \sigma^{(n-1)}(\bar{r}', \tau''', |\bar{E}^{(n-1)}|)\right\} \tag{9}$$

$$E_{\alpha}^{(n)}(\bar{r}', \tau') = -\frac{c\mu_0}{2}\frac{1}{r'}\int_0^{r'} dr'' r'' J_{\text{pri},\alpha}(\bar{r}'', \tau') \exp\left\{-\frac{c\mu_0}{2}\int_{r''}^{r'} dr''' \sigma^{(n-1)}(\bar{r}''', \tau', |\bar{E}^{(n-1)}|)\right\} \tag{10}$$

with $n = 2, 3, \ldots$, until $E^{(n)}$ converges. The convergent electric field is then substituted into Eq. (3) to obtain the convergent air conductivity. Then, Eq. (2) is applied to obtain the secondary current density over $\tau' \leq 1\,\mu$s.

4. COMPUTATION OF REFLECTED FIELD

The incident electric field at $\bar{r}_s$ on the ground surface, induced by the electric currents in the source region, can be computed by applying the Jefimenko's equation as [9]

$$\bar{E}_i(\bar{r}_s, t) = \frac{1}{4\pi\epsilon_0}\iiint_{V'} d\bar{r}_d \left[-\frac{\bar{J}(\bar{r}_d, t')}{cR^2} + 2\bar{R}\frac{\bar{J}(\bar{r}_d, t')\cdot\bar{R}}{cR^4} + \bar{R}\frac{\partial\bar{J}(\bar{r}_d, t')/\partial t'\cdot\bar{R}}{c^2R^3} - \frac{\partial\bar{J}(\bar{r}_d, t')/\partial t'}{c^2R}\right] \tag{11}$$

where $\bar{R} = \bar{r}_s - \bar{r}_d$ and $R = |\bar{R}|$. Eq. (11) can be transformed to the frequency domain as

$$\bar{E}_i(\bar{r}_s, \omega) = \frac{1}{4\pi\epsilon_0}\iiint_{V'} d\bar{r}_d \left[-\frac{\bar{J}(\bar{r}_d, \omega)}{cR^2} + 2\bar{R}\frac{\bar{J}(\bar{r}_d, \omega)\cdot\bar{R}}{cR^4} + \bar{R}\frac{j\omega\bar{J}(\bar{r}_d, \omega)\cdot\bar{R}}{c^2R^3} - \frac{j\omega\bar{J}(\bar{r}_d, \omega)}{c^2R}\right] e^{-j\omega R/c} \tag{12}$$

where

$$\bar{E}_i(\bar{r}_s, t) = \frac{1}{2\pi}\int_{-\infty}^{\infty} d\omega \bar{E}_i(\bar{r}_s, \omega) e^{j\omega t} \tag{13}$$

and the current density in the source region is transformed to

$$\bar{J}(\bar{r}_d, \omega) = e^{-j\omega r'/c}\bar{J}_0(\bar{r}_d, \omega) \tag{14}$$

with

$$\bar{J}_0(\bar{r}_d, \omega) = \int_0^{\infty} d\tau' \bar{J}(\bar{r}_d, \tau') e^{-j\omega\tau'} \tag{15}$$

By substituting Eq. (14) into Eq. (12), we have

$$\begin{aligned}\bar{E}_i(\bar{r}_s, \omega) = \frac{1}{4\pi\epsilon}\iiint_{V'} d\bar{r}_d \Bigg[&-\frac{\bar{J}_0(\bar{r}_d, \omega)}{cR^2} + 2\bar{R}\frac{\bar{J}_0(\bar{r}_d, \omega)\cdot\bar{R}}{cR^4} \\ &+ \bar{R}\frac{j\omega\bar{J}_0(\bar{r}_d, \omega)\cdot\bar{R}}{c^2R^3} - \frac{j\omega\bar{J}_0(\bar{r}_d, \omega)}{c^2R}\Bigg] e^{-j\omega(r'+R)/c}\end{aligned} \tag{16}$$

which can be further decomposed into TE and TM fields as

$$\bar{E}_i(\bar{r}_s, \omega) = \bar{E}_i^{\text{TE}}(\bar{r}_s, \omega) + \bar{E}_i^{\text{TM}}(\bar{r}_s, \omega) \tag{17}$$

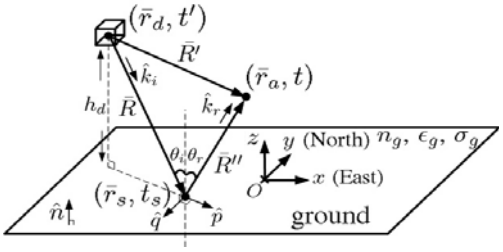

Figure 4. Incident and reflected fields near ground, attributed to currents in a small volume in the source region.

Figure 4 shows the schematic to compute the incident and reflected fields near ground, contributed by the currents in a small cube in the source region. The reflected field at $\bar{r}_s$ is the superposition of reflected TE and TM fields, which are obtained by multiplying the incident TE and TM fields with the corresponding reflection coefficients, respectively, namely,

$$\bar{E}_r(\bar{r}_s, \omega) = [\Gamma_{\rm TE}\hat{q}\hat{q} + \Gamma_{\rm TM}\,(\hat{p}\hat{p} - \hat{z}\hat{z})] \cdot \bar{E}_i(\bar{r}_s, \omega) \tag{18}$$

where $\hat{q} = \hat{x}\sin\theta_1 - \hat{y}\cos\theta_1$, $\hat{p} = \hat{x}\cos\theta_1 + \hat{y}\sin\theta_1$, with $\theta_1 = \cos^{-1}\left(R_x/\sqrt{R_x^2 + R_y^2}\right)$; and the reflection coefficients are represented as

$$\begin{aligned} \Gamma_{\rm TE}(\bar{r}_s, \bar{r}_d, \omega) &= \frac{k_{az} - k_{gz}}{k_{az} + k_{gz}} \\ \Gamma_{\rm TM}(\bar{r}_s, \bar{r}_d, \omega) &= \frac{j\omega\epsilon_0(k_{gz} - \epsilon_{rg}k_{az}) - \sigma_g k_{az}}{j\omega\epsilon_0(k_{gz} + \epsilon_{rg}k_{az}) + \sigma_g k_{az}} \end{aligned} \tag{19}$$

where $\theta_i = \theta_r = \cos^{-1}\left(-\hat{z}\cdot\hat{R}\right)$, $k_a = \omega\sqrt{\mu_0\epsilon_0}$, $k_g = \omega\sqrt{\mu_0\,(\epsilon_0\epsilon_{rg} - j\sigma_g/\omega)}$, $k_{az} = k_a\cos\theta_i$, $k_{ap} = k_a\sin\theta_i$, and $k_{gz} = \sqrt{k_g^2 - k_{ap}^2}$.

The reflected field at $\bar{r}_s$ can thus be expressed as

$$\bar{E}_r(\bar{r}_s, \omega) = \frac{1}{4\pi\epsilon_0}\iiint_{V'} d\bar{r}_d \bar{E}_{r0}(\bar{r}_s, \bar{r}_d, \omega) e^{-j\omega(r'+R)/c} \tag{20}$$

with

$$\begin{aligned} \bar{E}_{r0}(\bar{r}_s, \bar{r}_d, \omega) \;=\; & [\Gamma_{\rm TE}\hat{q}\hat{q} + \Gamma_{\rm TM}\,(\hat{p}\hat{p} - \hat{z}\hat{z})] \\ & \left[-\frac{\bar{J}_0(\bar{r}_d, \omega)}{cR^2} + 2\bar{R}\frac{\bar{J}_0(\bar{r}_d, \omega)\cdot\bar{R}}{cR^4} + \bar{R}\frac{j\omega\bar{J}_0(\bar{r}_d, \omega)\cdot\bar{R}}{c^2R^3} - \frac{j\omega\bar{J}_0(\bar{r}_d, \omega)}{c^2R}\right] \end{aligned} \tag{21}$$

Finally, the total electric field at $\bar{r}_a$ near ground can be represented as

$$\bar{E}(\bar{r}_a, t) = \bar{E}_i(\bar{r}_a, t) + \bar{E}_r(\bar{r}_a, t)$$

where

$$\begin{aligned} \bar{E}_r(\bar{r}_a, t) \;=\; & \frac{1}{4\pi\epsilon_0}\iiint_{V'} d\bar{r}_d \frac{1}{2\pi}\int_{-\infty}^{\infty} d\omega \bar{E}_{r0}(\bar{r}_s, \bar{r}_d, \omega) \\ & e^{j\omega[t-(r'+R+R'')/c]} = \frac{1}{4\pi\epsilon_0}\iiint_{V'} d\bar{r}_d \bar{E}_{r0}(\bar{r}_s, \bar{r}_d, \tau'') \end{aligned}$$

with $\tau'' = t - (r'+R+R'')/c$, $\bar{R}' = \bar{r}_a - \bar{r}_d$, $\bar{R}'' = \bar{r}_a - \bar{r}_s$, $R' = |\bar{R}'|$, $R'' = |\bar{R}''|$, and $\bar{k}_r\cdot\bar{R}'' = k_a R'' = \omega R''/c$.

5. SIMULATIONS AND DISCUSSIONS

We will simulate an explosion of 10 kiloton yield, which is ignited at 100 km above ground. The geomagnetic field is assumed to be $\bar{B}_0 = \hat{y}B_0$, with $B_0 = 0.4$ Gauss. The source region is divided into a finite number of cubes. The fields radiated from the induced currents at different cubes will arrive at the observation point with different time delays. The effective time duration of the early-time HEMP observed near ground is about 1 μs.

Figure 5 shows the time of the first arrival signals from cubes in the source region, with the observation point at $(x_a, y_a, z_a) = (0, 0, 10)$ m and the height-of-burst (HOB) at 100 km. The region contributing to the first 1 μs (333.3 μs $\leq t \leq$ 334.3 μs) of observed fields are highlighted with darker tone. The vertical range of the effective source region is determined by the magnitude of current density, which is in turns determined by the air density.

Figure 6 shows the temporal variation of air conductivity at $(x_a, y_a, z_a) = (0, 0, 19)$ km, with the molecular fraction of water vapor being set to $f_w = 0$. By applying (9) and (10) iteratively, the field-dependent air conductivity converges at $n \geq 7$, and its magnitude turns out to be more than 20 times higher than that computed without considering the field dependence.

Figure 7 shows the temporal variation of the x component of both the primary and the secondary

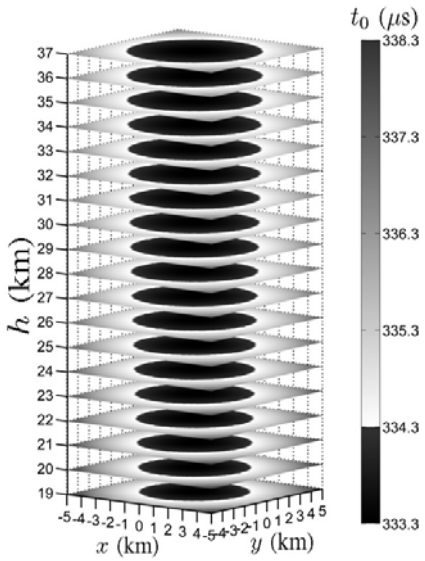

Figure 5. Time of the first arrival signals from cubes in the source region, the observation point is at $(x_a, y_a, z_a) = (0, 0, 10)$ m, and HOB = 100 km.

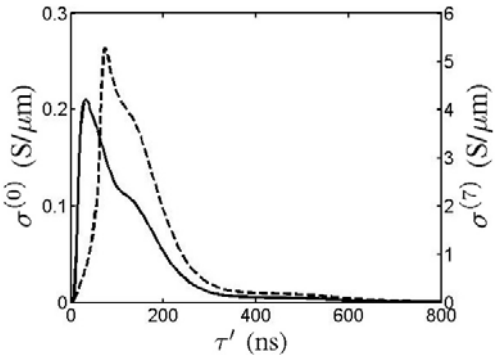

Figure 6. Temporal variation of air conductivity at $(x_a, y_a, z_a) = (0, 0, 19)$ km; ——: $\sigma^{(0)}$, − − −: $\sigma^{(7)}$, $f_w = 0$.

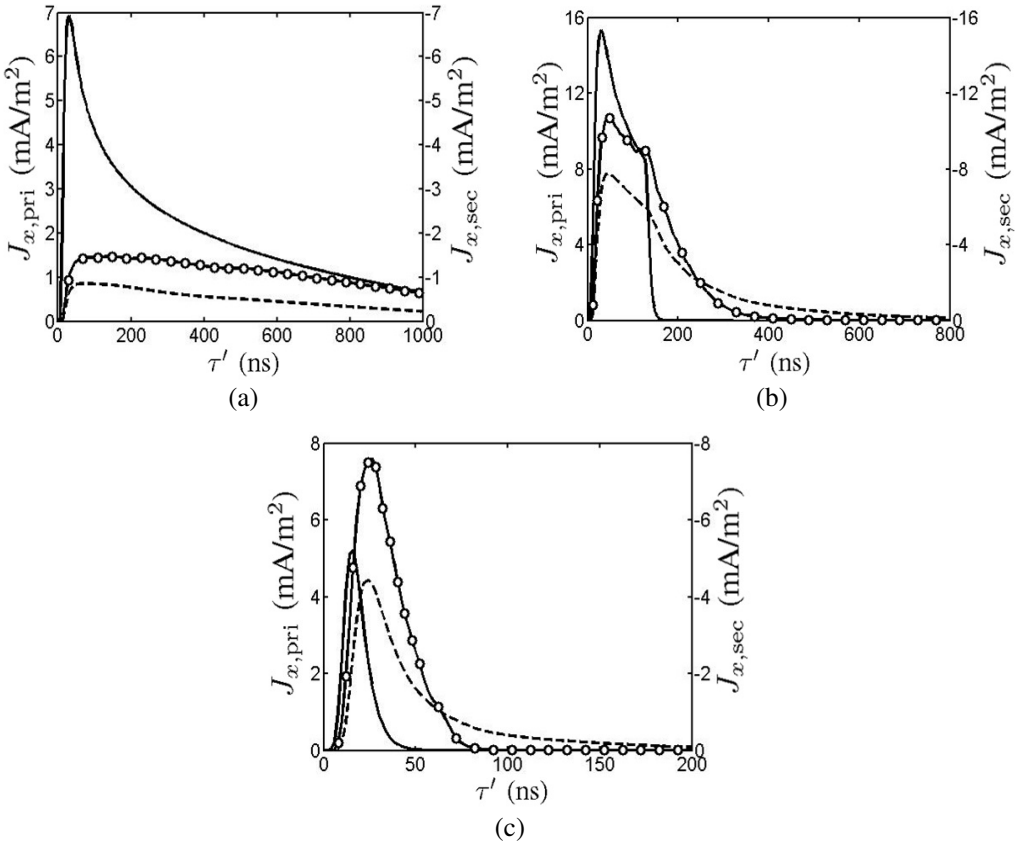

Figure 7. The x component of primary and secondary current densities, $f_w = 0$; ——: $J_{x,\mathrm{pri}}$, $- - -$: $J^{(0)}_{x,\mathrm{sec}}$, $-\circ-$: $J^{(7)}_{x,\mathrm{sec}}$. (a) $\bar{r}_a = (0, 0, 37)$ km, (b) $\bar{r}_a = (0, 0, 28)$ km, (c) $\bar{r}_a = (0, 0, 19)$ km.

current densities, at $\bar{r}_a = (0, 0, 37)$ km, $(0, 0, 28)$ km and $(0, 0, 19)$ km, respectively. The associated z components are shown in Fig. 8.

The secondary current density is computed as $J^{(n)}_{\alpha,\mathrm{sec}} = \sigma^{(n)} E^{(n+1)}_{\alpha}$, with $\alpha = x, z$. The current densities have negligible y component because the geomagnetic field points in the y direction. The secondary current density computed with the field-dependent air conductivity appears to be larger than that computed with field-independent air conductivity, and the former current density lasts longer than the latter one. The current densities at a higher altitude last longer because R_γ is larger at higher altitudes. The x component of the secondary current density is comparable to that of the primary one due to the strong transverse electric field.

In [6], the transverse incident field at $\bar{r}_a$ near ground was estimated as

$$\bar{E}_i(\bar{r}_a, t) = \bar{E}_b(\bar{r}'_b, \tau') \frac{r'_b}{r_a} \tag{22}$$

where $\bar{E}_b$ is the electric field at the bottom surface of the source region; $\bar{r}'_b$ is the intersection point of the line from O' to $\bar{r}_a$ and the bottom surface of the source region; r'_b and r_a are the distances from O' to $\bar{r}'_b$ and $\bar{r}_a$, respectively. Note that (22) is used only to estimate the magnitude and polarization of the impulse field.

Next, we will compute the transverse incident field at $\bar{r}_a$ by using the following four different approaches: (i) Compute the electric field $\bar{E}_b$ at the bottom of the source region, with field-independent air conductivity as in Eqs. (7) and (8), then apply the relation in Eq. (22) to compute $\bar{E}_i(\bar{r}_a, t)$. (ii) Compute the electric field $\bar{E}^{(1)}$ within the source region, with field-independent air conductivity as in Eqs. (7) and (8), obtain the secondary current density by using Eq. (2), then substitute both the primary and the secondary current densities into the Jefimenko's equation in Eq. (11) to compute $\bar{E}_i(\bar{r}_a, t)$. (iii)

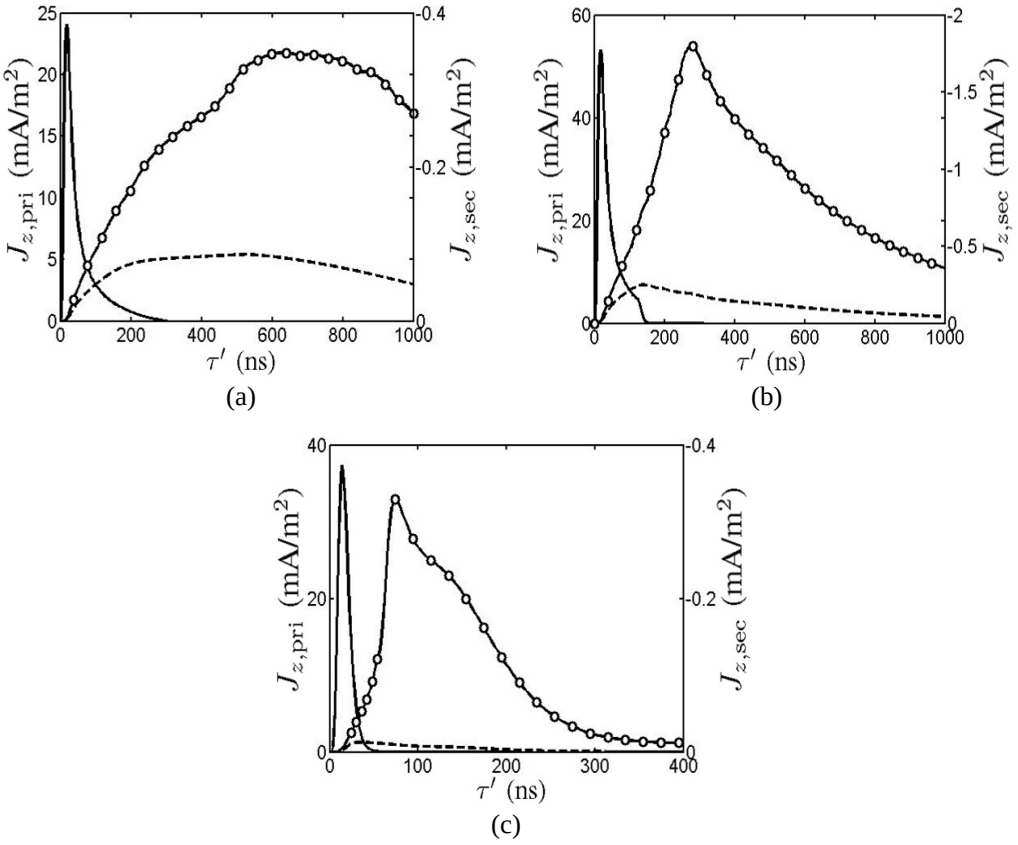

Figure 8. The z component of primary and secondary current densities, $f_w = 0$; ——: $J_{z,\mathrm{pri}}$, $- - -$: $J^{(0)}_{z,\mathrm{sec}}$, $-\circ-$: $J^{(7)}_{z,\mathrm{sec}}$. (a) $\bar{r}_a = (0, 0, 37)$ km, (b) $\bar{r}_a = (0, 0, 28)$ km, (c) $\bar{r}_a = (0, 0, 19)$ km.

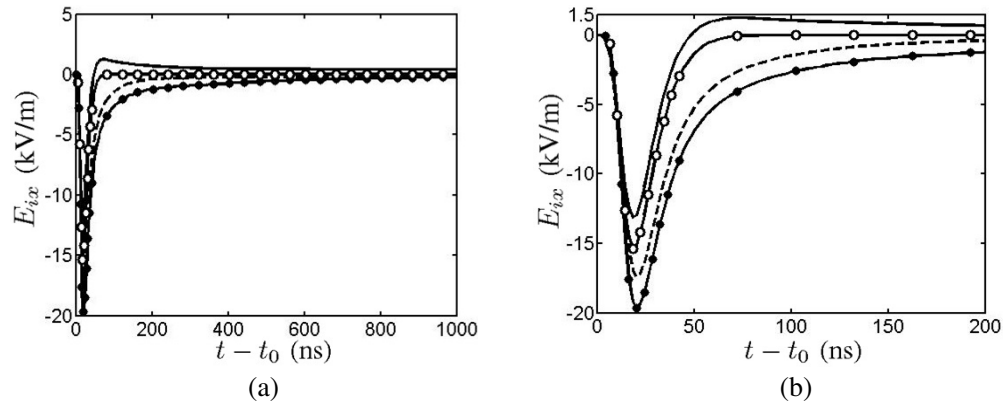

Figure 9. Waveforms of E_{ix} at $(x_a, y_a, z_a) = (0, 0, 10)$ m, $f_w = 0$, $t_0 = 333.3\,\mu$s. $-\bullet-$: approach (i), $- - -$: approach (ii), $-\circ-$: approach (iii), ——: approach (iv).

Compute the electric field $\bar{E}_b$ at the bottom of the source region, with field-dependent air conductivity as in Eqs. (9) and (10), then apply the relation in Eq. (22) to compute $\bar{E}_i(\bar{r}_a, t)$. (iv) Compute the electric field $\bar{E}^{(n)}$ within the source region, with field-dependent air conductivity as in Eqs. (9) and (10), obtain the secondary current density by using Eq. (2), then substitute both the primary and the secondary current densities into the Jefimenko's equation in Eq. (11) to compute $\bar{E}_i(\bar{r}_a, t)$. Similarly, the vertical incident field at $\bar{r}_a$ will also be computed by using approaches (ii) and (iv), respectively.

Figure 9 shows the waveforms of the transverse incident field E_{ix} at $(x_a, y_a, z_a) = (0, 0, 10)$ m, with $f_w = 0$. The peak values of E_{ix} obtained by using approaches (i) to (iv) are $-19,685$, $-17,413$, $-15,354$ and $-13,153$ kV/m, respectively. The peak value of E_{ix} obtained with the field-dependent air conductivity is smaller than its counterpart with the field-independent air conductivity by 4 kV/m. Note that by using approach (iv), the polarity of E_{ix} changes from negative to positive at about the time when the secondary current becomes larger than the primary current, as shown in Fig. 7. The E_{iy} component is close to zero because the geomagnetic field is polarized in the y direction.

Figure 10 shows the waveforms of E_{ix} at $(x_a, y_a, z_a) = (0, 0, 10)$ m, with $f_w = 0$, attributed to the primary and the secondary currents, respectively. Note that the right vertical axis increases downwards. The electric field induced by the secondary current obtained with field-dependent air conductivity is larger than that obtained with field-independent air conductivity.

Figure 11 shows the waveforms of the vertical incident field E_{iz} at $(x_a, y_a, z_a) = (0, 0, 10)$ m, with $f_w = 0$. The peak values of E_{iz} obtained by using approaches (ii) and (iv) are -35.2 V/m and -31.7 V/m, respectively. The secondary current obtained with field-dependent air conductivity is larger than its counterpart with field-independent air conductivity, leading to a faster decay of E_{iz} with time. The pulse width of the E_{ix} waveform is narrower than that of the E_{iz} waveform.

Figure 12 shows the waveforms of the vertical incident field E_{iz} at $(x_a, y_a, z_a) = (0, 0, 10)$ m, with $f_w = 0$, attributed to the primary and the secondary currents, respectively. Note that the right vertical axis increases downwards.

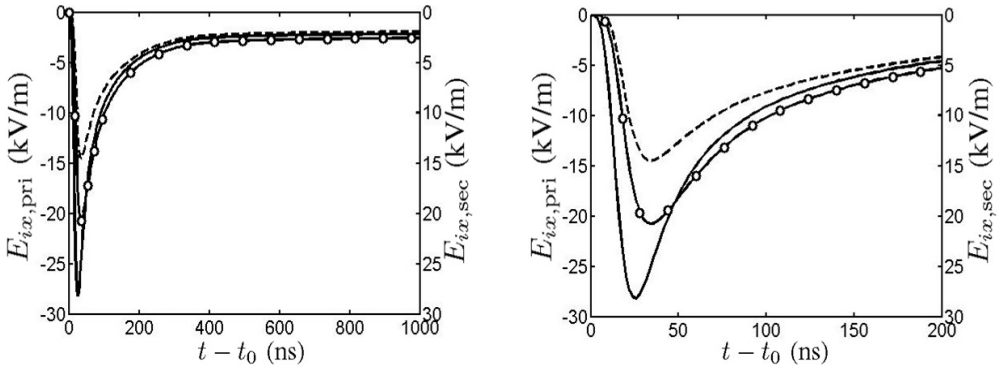

Figure 10. Waveforms of E_{ix} at $(x_a, y_a, z_a) = (0, 0, 10)$ m, $f_w = 0$, $t_0 = 333.3$ µs. ——: $E_{ix,\mathrm{pri}}$, − − −: $E^{(1)}_{ix,\mathrm{sec}}$, approach (ii), − ∘ −: $E^{(7)}_{ix,\mathrm{sec}}$, approach (iv).

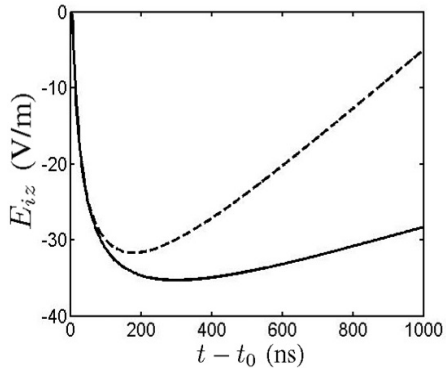

Figure 11. Waveforms of E_{iz} at $(x_a, y_a, z_a) = (0, 0, 10)$ m, $f_w = 0$, $t_0 = 333.3$ µs. ——: approach (ii), − − −: approach (iv).

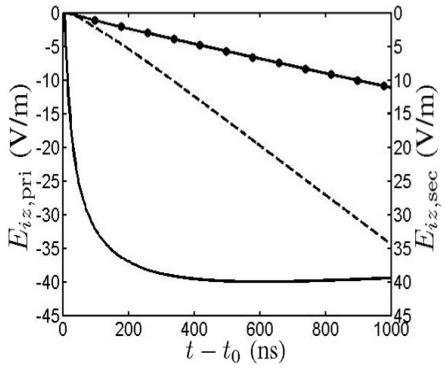

Figure 12. Waveforms of E_{iz} at $(x_a, y_a, z_a) = (0, 0, 10)$ m, $f_w = 0$, $t_0 = 333.3$ µs. ——: $E_{iz,\mathrm{pri}}$, − • −: $E^{(1)}_{iz,\mathrm{sec}}$, approach (ii), − − −: $E^{(7)}_{iz,\mathrm{sec}}$, approach (iv).

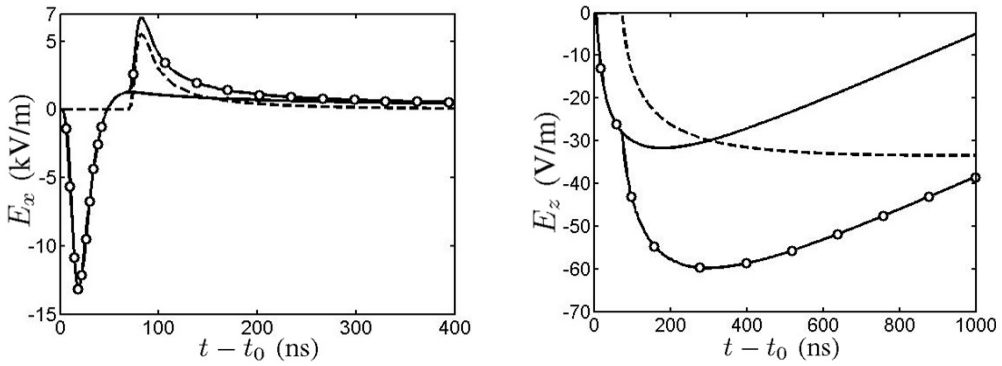

Figure 13. Waveforms of (a) E_{ix} (——), E_{rx} (− − −), E_{tx} (− ∘ −) and (b) E_{iz} (——), E_{rz} (− − −), E_{tz} (− ∘ −); at $(x_a, y_a, z_a) = (0, 0, 10)$ m, $t_0 = 333.3\,\mu$s.

Figure 13 shows the waveforms of the incident, reflected and total electric fields, respectively, at $(x_a, y_a, z_a) = (0, 0, 10)$ m, with a medium dry ground and $f_w = 0$. The peak values of E_{ix} and E_{rx} are $-13,153$ V/m and $5,517$ V/m, respectively; and the peak value of E_{iz} is -31.7 V/m. The field components observed at $t - t_0 > 100$ ns are attributed to the cubes in the source region away from the line-of-sight path. The polarity of E_{rx} is opposite to that of E_{ix} due to the ground reflection coefficient.

6. CONCLUSION

An iterative approach is proposed to determine the distribution of electric field and field-dependent air conductivity in the source region. The Jefimenko's equation is then applied to compute the HEMP waveform near ground, induced by the primary and the secondary current densities in the source region. The reflected waveform is computed in the frequency domain, in which the frequency dependence of ground permittivity is incorporated. The field-dependent air conductivity in the source region is 20 times higher than that computed without considering the field dependence. The electric fields, observed near ground, contributed by cubes in the source region aside from the line-of-sight path can be significant and last much longer than the impulse duration.

REFERENCES

1. Ianoz, M., "A review of HEMP activities in Europe," *IEEE Trans. Electromagn. Compat.*, Vol. 55, No. 3, 412–421, Jun. 2013.
2. Karzas, W. J. and R. Latter, "Detection of the electromagnetic radiation from nuclear explosions in space," *Phys. Rev.*, Vol. 137, No. 5B, 1369–1378, 1965.
3. Longmire, C. L., "On the electromagnetic pulse produced by nuclear explosions," *IEEE Trans. Electromagn. Compat.*, Vol. 20, No. 1, 3–12, Feb. 1978.
4. Roussel-Dupre, R. A., "Prompt nuclear EMP and synchrotron radiation: A resolution of two approaches," *IEEE Trans. Electromagn. Compat.*, Vol. 47, No. 3, 552–558, Aug. 2005.
5. Eng, C. D., "Development of the time dependence of the nuclear (E1) HEMP electric field," *IEEE Trans. Electromagn. Compat.*, Vol. 53, No. 3, 737–748, Aug. 2011.
6. Meng, C., "Numerical simulation of the HEMP environment," *IEEE Trans. Electromagn. Compat.*, Vol. 55, No. 3, 440–445, Jun. 2013.
7. Seiler, Jr., L. W., "A calculational model for high altitude EMP," Air Force Inst. Technol., Wright-Patterson Air Force Base, Ohio, Mar. 1975.
8. Baum, C. E., "Electron thermalization and mobility in air," EMP Theoretical Note, 12, Jul. 1965.
9. Jefimenko, O. D., *Electromagnetic Retardation and Theory of Relativity*, Electret Scientific, 2004.